Open access • Journal Article • DOI:10.1002/2013JA019387

Thermospheric Dissipation of Upward Propagating Gravity Wave Packets

C. J. Heale, Jonathan B. Snively, Michael P. Hickey, C. J. Ali

Institutions: Embry-Riddle Aeronautical University, Daytona Beach

Published on: 01 May 2014 - Journal of Geophysical Research (John Wiley & Sons, Ltd)

Topics: Surface wave, Wave packet, Wavelength, Capillary wave and Dissipation

5-12-2014

Thermospheric Dissipation of Upward Propagating Gravity Wave Packets

C. J. Heale
Embry-Riddle Aeronautical University, HEALEC@erau.edu

J. B. Snively
Embry-Riddle Aeronautical University, snivelyj@erau.edu

M. P. Hickey
Embry-Riddle Aeronautical University, hicke0b5@erau.edu

C. J. Ali
Embry-Riddle Aeronautical University, ALIC@my.erau.edu

Scholarly Commons Citation

Heale, C. J., Snively, J. B., Hickey, M. P., & Ali, C. J. (2014). Thermospheric Dissipation of Upward Propagating Gravity Wave Packets. *Journal of Geophysical Research: Space Physics, 119*(5). https://doi.org/10.1002/2013JA019387

AGU PUBLICATIONS

JGR

Journal of Geophysical Research: Space Physics

RESEARCH ARTICLE

10.1002/2013JA019387

Key Points:
- Dispersion of a GW packet leads to selective dissipation of spectral components
- The dominant vertical wavelength of a packet decreases in time while dissipating
- At an instant in time, vertical wavelength of a packet increases in altitude

Correspondence to:
C. J. Heale,
healec@my.erau.edu

Citation:
Heale, C. J., J. B. Snively, M. P. Hickey, and C. J. Ali (2014), Thermospheric dissipation of upward propagating gravity wave packets, *J. Geophys. Res. Space Physics*, *119*, 3857–3872, doi:10.1002/2013JA019387.

Received 11 SEP 2013
Accepted 10 APR 2014
Accepted article online 14 APR 2014
Published online 12 MAY 2014

Thermospheric dissipation of upward propagating gravity wave packets

C. J. Heale[1], J. B. Snively[1], M. P. Hickey[1], and C. J. Ali[1]

[1]Department of Physical Sciences, Embry-Riddle Aeronautical University, Daytona Beach, Florida, USA

Abstract We use a nonlinear, fully compressible, two-dimensional numerical model to study the effects of dissipation on gravity wave packet spectra in the thermosphere. Numerical simulations are performed to excite gravity wave packets using either a time-dependent vertical body forcing at the bottom boundary or a specified initial wave perturbation. Three simulation case studies are performed to excite (1) a steady state monochromatic wave, (2) a spectrally broad wave packet, and (3) a quasi-monochromatic wave packet. In addition, we analyze (4) an initial condition simulation with an isothermal background. We find that, in cases where the wave is not continually forced, the dominant vertical wavelength decreases in time, predominantly due to a combination of refraction from the thermosphere and dissipation of the packets' high frequency components as they quickly reach high altitude. In the continually forced steady state case, the dominant vertical wavelength remains constant once initial transients have passed. The vertical wavelength in all simulations increases with altitude above the dissipation altitude (the point at which dissipation effects are greater than the wave amplitude growth caused by decreasing background density) at any fixed time. However, a shift to smaller vertical wavelength values in time is clearly exhibited as high-frequency, long vertical wavelength components reach high altitudes and dissipate first, to be replaced by slower waves of shorter vertical wavelength. Results suggest that the dispersion of a packet significantly determines its spectral evolution in the dissipative thermosphere.

1. Introduction

Gravity waves are ubiquitous in the Earth's mesosphere and lower thermosphere (MLT) and are acknowledged to have a major role in the dynamics of this region [*Oliver et al.*, 1997; *Fritts and Alexander*, 2003; *Djuth et al.*, 2004]. Following the pioneering work of *Hines* [1960], one of the main effects of gravity waves was found to be the transport of energy and momentum from source regions, typically in the troposphere [*Hung and Kuo*, 1978; *Kelley*, 1997; *Hocke and Tsuda*, 2001], to higher regions of the atmosphere, where dissipation becomes important. Due to conservation of energy, a wave's amplitude increases as the atmospheric density decreases in a nonviscous atmosphere as long as the wave remains of small linear amplitude. However, the effects of molecular viscosity simultaneously increase with decreasing density and counteract the growth of the wave. In the lower thermosphere the molecular viscosity can become sufficient for dissipation to overtake the growth of the wave, such that its amplitude will decline as its energy and momentum are deposited to the mean state. The effectiveness and time scales of damping by molecular viscosity are functions of a particular wave's phase speed and spatial scale. Alternatively, if the wave reaches a sufficiently large amplitude, wave breaking or wave-wave interactions can occur resulting in nonlinear deposition of energy and momentum into the mean flow [*Fritts et al.*, 2006; *Yigit et al.*, 2008, 2009; *Fritts and Lund*, 2011].

The effects of dissipation on gravity wave dynamics have been investigated by a number of studies, utilizing different approaches that include ray tracing or numerical modeling [*Zhang and Yi*, 2002; *Vadas and Fritts*, 2005; *Yu et al.*, 2009; *Hickey et al.*, 2010, 2011; *Liu et al.*, 2013; *Walterscheid*, 2013]. Studies of gravity waves in the MLT suggest that the lower thermosphere can act as a barrier to upward energy propagation. It is known that waves of different scales dissipate at different altitudes, leading to an atmospheric filtering effect, where longer-wavelength/shorter-period waves reach the highest altitudes [*Pitteway and Hines*, 1963; *Francis*, 1973; *Vadas*, 2007]. Thus, waves of different intrinsic properties will deposit their energy at different altitudes. It has been suggested that the increasing molecular kinematic viscosity with altitude may act to shorten the dominant vertical wavelength in an isothermal atmosphere, resulting in a more horizontal trajectory and a maximum altitude of energy propagation in the lower and midthermosphere [e.g., *Zhang and Yi*, 2002]. It has also been found that the momentum deposited during wave dissipation can cause a body

forcing which excites secondary waves. These waves can propagate up to 500 km in altitude before they then dissipate [*Vadas*, 2007; *Vadas and Liu*, 2009, 2013].

Vadas and Fritts [2005] derived an anelastic dispersion relation which includes molecular viscosity and thermal diffusivity as well as deriving the corresponding ray tracing equations. They found that high phase velocity gravity waves, with large vertical wavelength, dissipate at the highest altitudes. In some cases, initially large vertical wavelengths were found to decrease significantly by the time the waves dissipated. In particular, it was found that λ_z decreased above the dissipation altitude for a time-varying wave packet under isothermal conditions, when tracing the path of the packet as described by its group velocity.

Reduction of vertical wavelengths was also reported by *Liu et al.* [2013], using a 2-D nonlinear, compressible numerical model, who analyzed an isolated packet as it dissipated in both isothermal and nonisothermal atmospheres. They also note the competing effects of background temperature and molecular viscosity, which act to increase and decrease the vertical wavelength, respectively, in a nonisothermal case study.

In contrast, *Hickey et al.* [1998] utilized a full-wave model (FWM) simulating a one-dimensional, monochromatic, steady state forcing, and found the vertical wavelength to always increase with altitude under the effects of dissipation. As a further complication to interpretation, *Waterscheid and Hickey* [2011] suggest that group velocity, which forms a large part of the ray tracing formalism, becomes a meaningless measure of vertical energy flow, while gravity waves are propagating in the lower thermosphere and are subject to dissipation. They also noted that ray tracing is derived from the WKB approximation which assumes slow-varying background fields as compared to the gravity wave vertical wavelengths [*Einaudi and Hines*, 1971]. Recent results also suggest that ray tracing may require understanding of the nature of the wave packet's localization and thus bandwidth, especially under dissipative conditions [*Walterscheid*, 2013].

In response, *Vadas and Nicolls* [2012] suggest that the two approaches are fundamentally different and do not yield the same solution. While *Vadas and Fritts* [2005] assume a complex wave frequency (ω) and considers time-dependent and spatially localized waves, the FWM employs a steady state, horizontally homogeneous approach with complex k_z, and constant forcing and energy inputs. It is suggested by *Vadas and Nicolls* [2012] that it is unclear if a Fourier series summation of real ω steady state solutions will yield accurate altitude solutions to time-dependent Navier stokes equations, and whether this approach is accurate when used to study transient wave packets. A physical explanation of the difference in the results is given in paragraph 13 of *Vadas and Nicolls* [2012].

This paper uses a fully compressible, nonlinear 2-D numerical model, adapted from *Snively and Pasko* [2008] and *Snively* [2013], to investigate the nature of wave packet dissipation, for spectrally broad, steady state, and intermediate scenarios by simulating three conditions: (1) a spectrally narrow, continuously forced wave (creating a steady state condition), (2) a spectrally broad gravity wave packet, created with spatially isolated forcing, and (3) a quasi-monochromatic gravity wave packet. We also compare with (4) an initial condition wave packet, similar to that of *Liu et al.* [2013], to investigate its time-dependent dissipation.

2. Numerical Model

2.1. Governing Equations and Background State

The numerical model utilizes a modified set of the Clawpack libraries [*LeVeque and Berger*, 2004], in the form described fully by *Snively and Pasko* [2008]. The equations solved are the nonlinear, fully compressible, Euler equations with the inclusion of two separately solved equations describing molecular viscosity and thermal conductivity.

Conservation of mass

$$\frac{\partial \rho}{\partial t} + \nabla \cdot (\rho \mathbf{v}) = 0 \tag{1}$$

Conservation of momentum

$$\frac{\partial}{\partial t}(\rho \mathbf{v}) + \nabla \cdot (\rho \mathbf{v}\mathbf{v}) = -\nabla p - \rho \mathbf{g} \tag{2}$$

Conservation of energy

$$\frac{\partial E}{\partial t} + \nabla \cdot (E + p)\mathbf{v} = -\rho g v_z \tag{3}$$

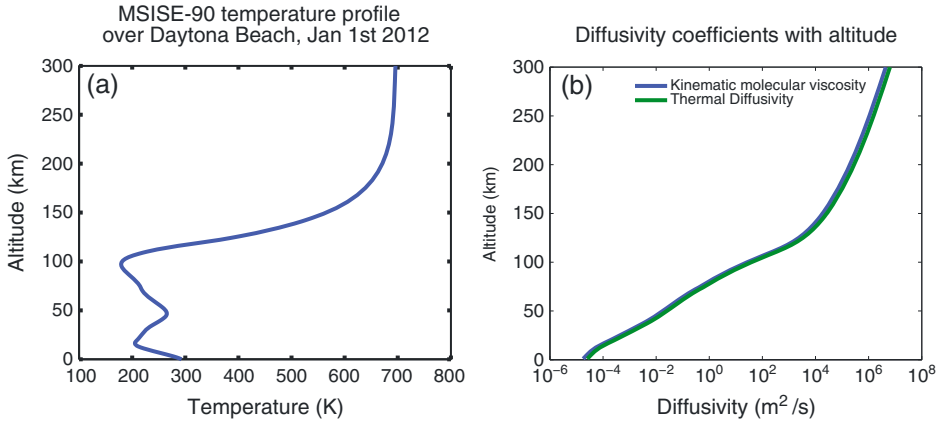

Figure 1. Plot of the (a) MSISE-90 temperature profile for the time-dependent forcings and (b) the dissipative coefficients with altitude for the MSIS-90E temperature simulations.

Equation of state

$$E = \frac{p}{(\gamma - 1)} + \frac{1}{2}\rho(\mathbf{v} \cdot \mathbf{v}) \tag{4}$$

Dissipation by molecular and thermal diffusion, accounting for the same processes described by the ray tracing model of *Vadas and Fritts* [2005], is applied via time splitting using an explicit forward difference method to solve the "heat" equations:

$$\frac{\partial \mathbf{v}}{\partial t} - \nu \nabla^2 \mathbf{v} = 0 \tag{5}$$

$$\frac{\partial T}{\partial t} - \kappa \nabla^2 T = 0 \tag{6}$$

where $\mathbf{v}$ is the velocity, ρ and p are density and pressure, T is temperature, g is the acceleration due to gravity, γ is the ratio of specific heats, and E is total energy. Note that no sponge layer or Rayleigh friction is used.

To account for the effects of varying composition in the lower thermosphere, we define the ratio of specific heats, γ, using an average of the monatomic and diatomic specific heats as described by *Walterscheid and Hickey* [2001]:

$$\gamma = \frac{5[\mathrm{O}] + 7([\mathrm{N_2}] + [\mathrm{O_2}])}{3[\mathrm{O}] + 5([\mathrm{N_2}] + [\mathrm{O_2}])} \tag{7}$$

This differs by only a few percent at lower thermospheric altitudes in comparison to approximations used by *Vadas* [2007] or *Snively and Pasko* [2008], and sensitivity tests confirm that all results are closely comparable. The specific gas constant R_{specific} is also specified to vary with composition

$$R_{\mathrm{specific}} = R_{\mathrm{ideal}} \frac{([\mathrm{N_2}] + [\mathrm{O_2}] + [\mathrm{O}])}{16[\mathrm{O}] + 28[\mathrm{N_2}] + 32[\mathrm{O_2}]} \tag{8}$$

The kinematic molecular viscosity and thermal conductivity are ν and κ, respectively, with the kinematic molecular viscosity ($\mathrm{m^2/s}$) set to match that of *Hickey et al.* [1998], given by the expression of *Rees* [1989]:

$$\nu = \frac{1}{\rho_0} \frac{3.43[\mathrm{N_2}] + 4.03[\mathrm{O_2}] + 3.90[\mathrm{O}]}{([\mathrm{N_2}] + [\mathrm{O_2}] + [\mathrm{O}])} T_0^{0.69} 10^{-7} \tag{9}$$

Here ρ_0 and T_0 are the background density and temperature, and the molecules in square brackets represent the number densities. The thermal conductivity is related to the molecular viscosity via the Prandtl number $Pr = \nu/\kappa$, which is set to 0.7. The diffusivities used in the simulations are shown in the Figure 1b.

Table 1. Model Dissipation Altitudes for the Various Forcing Cases

	SS	QM	SB
u peak altitude (km)	127	124	152
w peak altitude (km)	134	134	188
$\overline{u'w'}$ peak (km)	129	129	166

The background temperature used in the time-dependent simulations was obtained using the MSISE-90 empirical model [*Hedin*, 1991], set to Daytona Beach at 0 LT on 1 January 2012. The temperature profile is shown in Figure 1a.

2.2. Numerical Domain and Forcing

The numerical domain for the time-dependent simulations was specified to be 100 km in the x direction (horizontal) and 300 km in the z direction (vertical), with a resolution of 0.5 km in both cases. Results were output every 15 s, with a time step size of ~0.66 s for a Courant-Friedrichs-Lewy number of 0.5. The side boundaries were set to be periodic, with a reflective bottom boundary (at ground) and an open top boundary. A vertical body forcing was applied to the bottom boundary as given by

$$F_z(x,z,t) = Ae^{-0.5((z-z_c)^2/\sigma_z^2)} \times e^{-(t-t_c)^2/2\sigma_t^2} \sin(\omega(t-t_c) - k(x-x_c)) \quad (10)$$

In each of the simulations, the spatial parameters of the forcing were the same and produced a Gaussian modulated sine wave. Parameters are $A = 5\times10^{-6}$ N/kg, y_z=0, $\sigma_z = 3$ km, and $k = 2\pi/\lambda_x$ where, $\lambda_x = 100$ km and are summarized in Table 1. This produces exactly one horizontal wavelength in the domain which, due to the periodic boundary, gives an effectively infinite domain in x and spectrally isolates the 100 km horizontal mode. The amplitude was chosen to be small enough that it limits nonlinear interactions.

The time varying component of the forcing differed for each of the three simulations. For the quasi-monochromatic (QM) case, $t_c = 4\tau$, and $\sigma_t = \tau$, where $\tau = 30$ min (the period of the wave) and $\omega = \frac{2\pi}{\tau}$. For the spectrally broad (SB) packet, $t_c = 2\tau$, $\sigma_t = \frac{\tau}{4}$, where τ and ω have the same definition as before. The steady state (SS) case is forced in a piecewise manner where its forcing takes the form of equation (10) with $t_c = 4\tau$, and $\sigma_t = \tau$, where $\tau = 30$ min (the period of the wave) and $\omega = \frac{2\pi}{\tau}$ for $t \le t_c$. For $t > t_c$ the forcing takes the form

$$F_z(x,z,t) = Ae^{-0.5((z-z_c)^2/\sigma_z^2)} \times \sin(\omega(t-t_c) - k(x-x_c)) \quad (11)$$

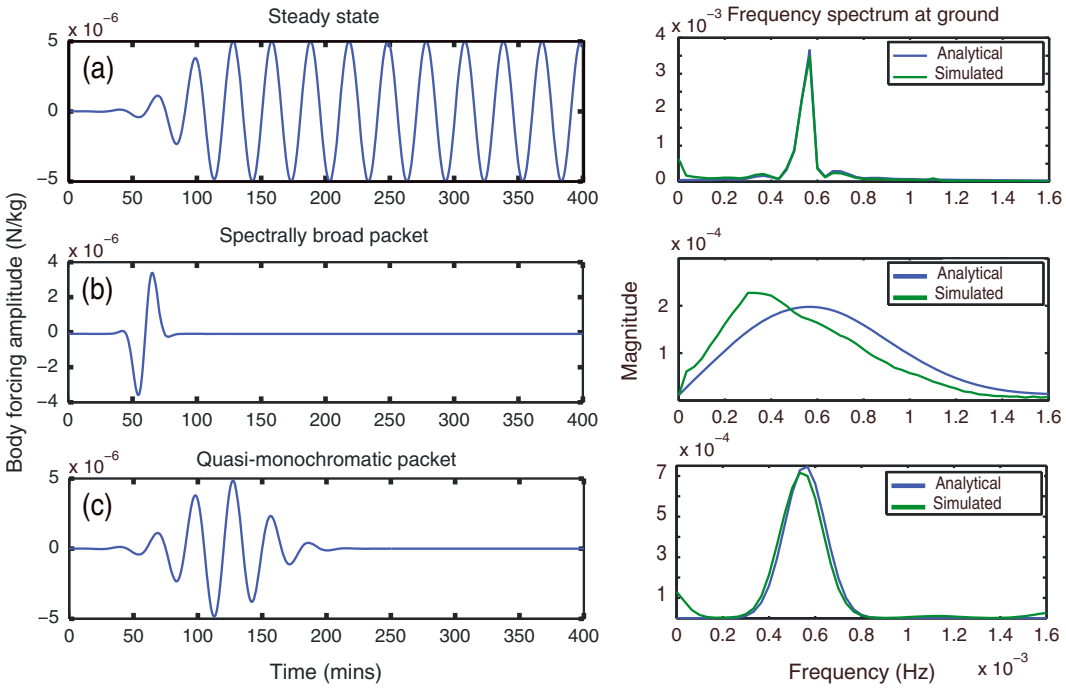

Figure 2. (left) The time-dependent components of the body forcing for each of the three simulations, as described in equations (10) and (11). (right) The corresponding frequency spectrum excited at $z = 0$ km.

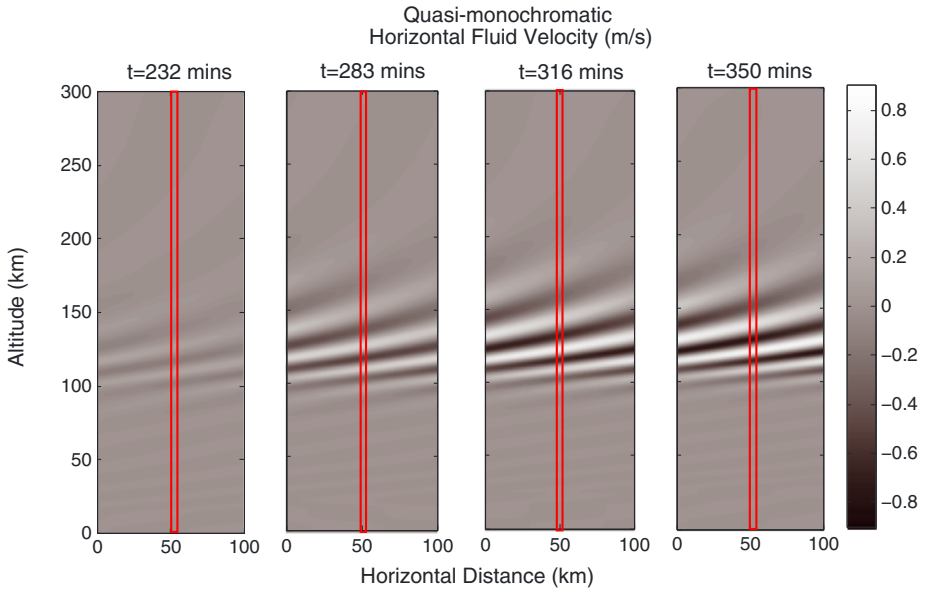

Figure 3. The horizontal wind of the quasi-monochromatic simulation at $t = 232$, 283, 316, and 350 min. The red box indicates where the vertical slice (for Figure 4) was taken.

where $\omega = \frac{2\pi}{\tau}$ and $\tau = 30$ min. The time-dependent parts of the forcing are shown in Figure 2, along with the corresponding frequency spectra at ground which is obtained by Fourier transform. No background winds were included in any of the simulations.

3. Results and Analysis

3.1. Gravity Wave Propagation

Figure 3 shows the unscaled horizontal wind output of the quasi-monochromatic forcing simulation at $t = 232$, 283, 316, and 350 min. The gravity wave packet does not travel very far over this time span. Its central position and extent remains relatively unchanged in the vertical, while the phase continues to progress and the amplitude increases. This same effect is seen in *Zhang and Yi* [2002], where the packet ceases to propagate vertically, and the group velocity becomes nearly exclusively horizontal when it reaches its dissipation altitude.

In order to investigate the time evolution of the gravity wave propagation, a vertical slice was taken at $x = 50$ km (denoted by the red rectangle in Figure 3) from the simulation at each time step. Each slice was then placed adjacent to each over in columns to produce a time evolution plot. Figure 4 shows each of the three simulations after the slices have been placed next to each other to illustrate the effect that the thermosphere has on a gravity wave as it propagates. The vertical spreading of the different packets is

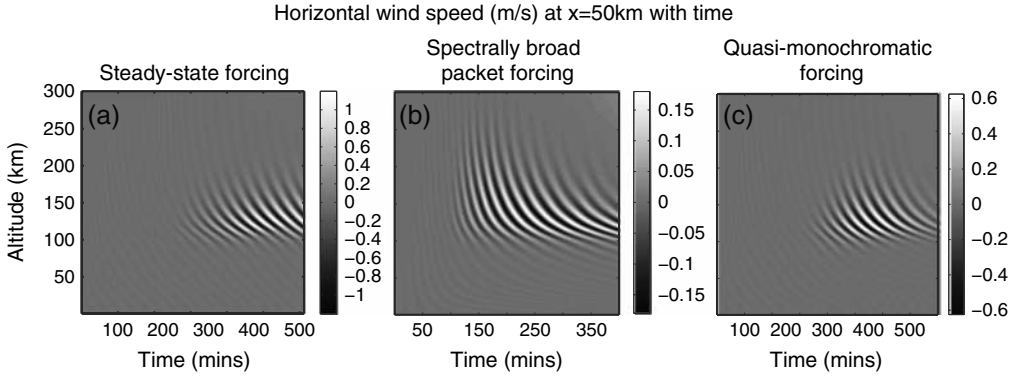

Figure 4. (a–c) The evolution of the horizontal wind with time for each gravity wave simulation case, produced by stacking vertical slices of the domain, each taken at $x = 50$ km, into columns.

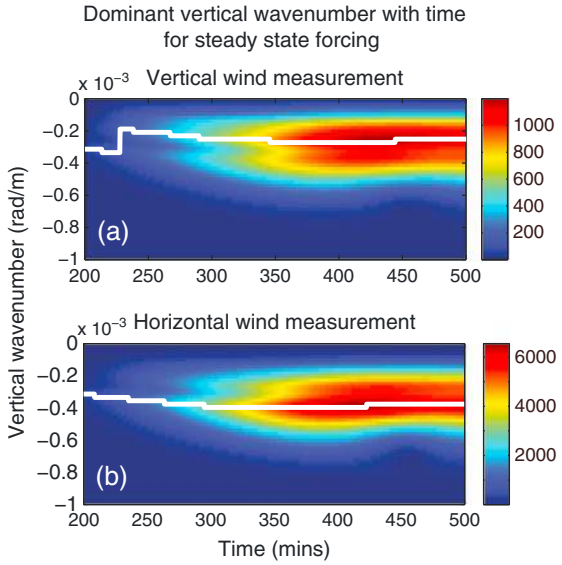

Figure 5. The evolution of the vertical wave number with time for the steady state forcing case. Derived (a) from the vertical wind and (b) from the horizontal wind. The overlaying white line indicates the maximum spectral intensity with time. It shows that the vertical wave number settles toward a constant value when the simulation reaches steady state.

very apparent, with the spatially broad packet dispersing the most due to its rich spectral content. It is also clear from the time evolution of the spectrally broad packet that the high frequency components (those with highly vertical phase fronts) reach the highest altitudes and dissipate first, leaving the slower, lower, frequency components (with more-horizontal phase fronts) to become dominant at later times in the simulation. Thus, the dominant spectral components change dramatically with the evolution of the wave. In this case, if tracking the dominant vertical wavelength in time, the vertical wavelength would appear to decrease. In the steady state simulation, energy is being constantly added to the system, as such the wave is present throughout the atmosphere (up to where the wave dissipates), and the wave field does not change significantly in time once a steady state has been reached. Also, for the steady state case, a single frequency component will dominate at late times, unlike the case of a packet whose position, span, and dominant frequency is time dependent. The quasi-monochromatic case, as expected, lies somewhere in between these two, in which the frequency content is broader than the steady state case but narrower than the spectrally broad case. Beyond 450 min, the quasi-monochromatic (QM) packet has significantly dissipated, and shorter vertical wavelengths become dominant. Already, this highlights a difference between steady state solutions such as *Hickey et al.* [1998] and more spatially isolated gravity wave packets such as those investigated by *Vadas* [2007], *Vadas et al.* [2009], and *Liu et al.* [2013].

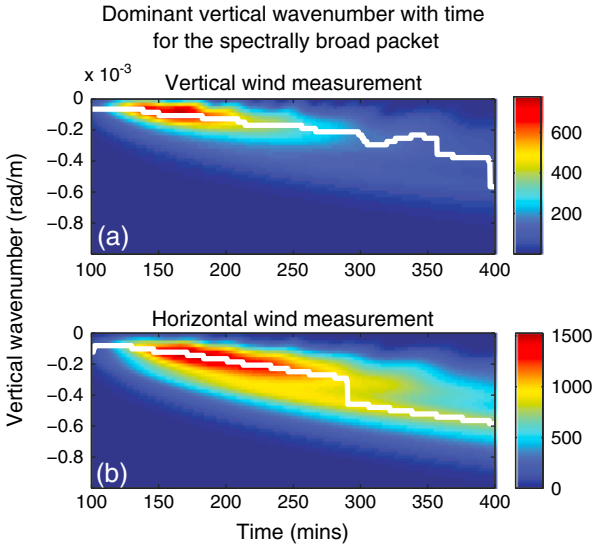

Figure 6. The evolution of the vertical wave number with time for the spectrally broad forcing case. Derived (a) from the vertical wind and (b) from the horizontal wind. The overlaying white line indicates the maximum spectral intensity with time. It shows a strong shortening of the vertical wavelength with time, unlike the steady state case.

3.2. Fourier Analysis of Vertical Wave Number and Wavelength

Following a similar analysis of *Zhang and Yi* [2002] and *Liu et al.* [2013], we take a 2-D Fourier transform of the simulation domain at each time step to obtain a spectrum and components in k_x and k_z wave number space. We then isolate the 100 km horizontal wavelength component, which is the dominant mode allowed by the simulation space, and stack this in time. This allows us to track the vertical wave number spectra in time and track the evolution of the dominant vertical wavelength of the packet. Figure 5 shows the evolution of the dominant vertical wave number with time for the steady state forcing. The vertical wave numbers are negative, which indicate an upward group velocity. An increasingly negative vertical wave number denotes a decrease in

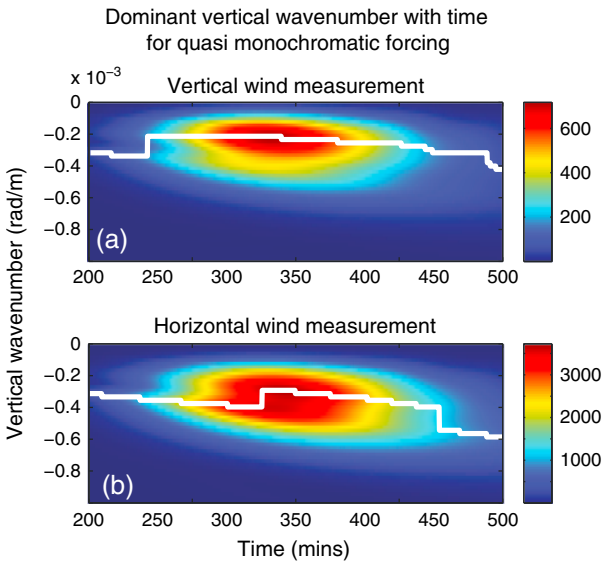

Figure 7. The evolution of the vertical wave number with time for the quasi-monochromatic forcing case. Derived (a) from the vertical wind and (b) from the horizontal wind. The overlaying white line indicates the maximum spectral intensity with time.

vertical wavelength. In the steady state case, we see a relatively small initial vertical wave number as the high-frequency portions of the spectrum and transients reach the highest altitudes and are initially dominant. As time progresses, the vertical wave number becomes increasingly negative and reaches a constant value as the simulation reaches its steady state, and the transients dissipate away. In the steady state case, we do not see a decrease in vertical wavelength with time. It is also worth noting that the vertical wave numbers derived from the horizontal and vertical wind velocities are different as expected based upon the study of *Einaudi and Hines* [1971]. In the horizontal wind measurement the dominant vertical wavelength converges to a value of 16 km, whereas it converges to 25 km when derived from the vertical wind. This occurs because the relative magnitudes of the horizontal and vertical winds are dependent upon the angle of phase propagation, which varies with altitude due to the varying background atmosphere and also due to the changing spectral content of the packet.

Figure 6 shows the evolution of the spectrally broad packet forcing. In this case there is a continuous decrease in the vertical wavelength with time, and the result reflects that of *Zhang and Yi* [2002] and *Liu et al.* [2013]. When there is a broad spectrum of waves excited, we see the largest change in vertical wave number of the three cases, as the packet evolves. At 100 min, the vertical wavelength derived from vertical wind is 100 km, and 75 km when derived from the horizontal wind. The peak in the spectrum comes at 168 min and 171 min, with a wavelength of 60 and 42 km, respectively, for the vertical and horizontal winds. Finally, at 300 min, the vertical wavelengths are reduced to 30 km and 13.6 km for the vertical and horizontal winds, respectively. We suggest this is due to a shift in the central frequency of the packet itself as the high frequency, longer wavelengths dissipate first and the lower frequency, shorter wavelength components become dominant as time proceeds. For reference, this is what is seen in Figure 4b as the longer wavelength, high frequency components are dominant early on in the simulation (and reach a higher altitude). They then dissipate first and make way for the slower, shorter wavelength waves which become dominant later in the simulation (and at lower altitudes). The fact that the dominant region of the wave shifts from higher to lower altitudes is consistent with this explanation and is the prominent (but not necessarily the only) observable cause of the decreasing vertical wavelength with time for this case.

Figure 7 shows a case which is intermediate to the two former cases. The quasi-monochromatic forcing is spectrally more narrow band than the broad packet case. Of the three, this is the case which is most similar to previous numerical studies [e.g., *Zhang and Yi*, 2002; *Liu et al.*, 2013] and provides the best comparison. We still see a steady decrease in the vertical wavelength with time after the transients decay (around 250 min) but not as much as in the spectrally broad case. There is also a noticeable switch in the vertical wavelength at 325 min, and then again, at 454 min in the horizontal wind measurement. This occurs due to a change in the dominant period of the packet at these times (at an altitude of 120 km; see Figure 9c). At 275 min, the vertical wavelength values are 30 km and 16 km as derived from the vertical and horizontal winds, which are similar to the spectrally broad values at the same time. The spectral intensity peaks at $\sim$342 min with λ_z values of 30 and 21 km, respectively, for vertical and horizontal winds. By 400 min, the corresponding vertical wavelengths have decreased to 25 and 17.6 km, respectively. Beyond this time, the spectral power decreases rapidly, and Figure 4c shows that the wave amplitude is decaying noticeably, indicating strong dissipation. Here we see a more rapid shortening of the vertical wavelength as the longer wavelengths (higher frequency) dissipate away, and the shorter wavelengths (lower frequency) packet

Table 2. Time-Dependent Forcing Parameters for the Three Simulations, Used in Equations (10) and (11)

	SS ($t \leq t_c$)	QM	SB
τ (min)	30	30	30
t_c (min)	120	120	60
σ_t (min)	30	30	7.5

components become more dominant. At the end of the simulation the vertical wavelengths have decreased to 15 km and 10.7 km for the vertical and horizontal wind measurements, respectively.

From the three different simulations, it appears that the amount of decrease in vertical wavelength with time is dependent upon the forcing used and, in particular, the breadth of the spectrum excited. It is noted that the atmosphere is nonisothermal and that background temperature affects the vertical wavelength also; however, the dominant factor in causing the vertical wavelength to decrease appears to be the earlier dissipation of the higher frequency components, as they reach the higher, more viscous atmosphere ahead of the slower, lower frequency waves.

3.3. Momentum Flux

The momentum flux (per unit density) is given by

$$f = \overline{u'w'} \tag{12}$$

where the overline denotes an average taken over the horizontal wavelength. Since our simulation is periodic, this calculation is simply summed over the horizontal domain at each altitude, divided by the (fixed) horizontal wavelength. Tracking the altitude of the peak value of the momentum flux with time gives an indication of where the dominant (most energetic) portion of the gravity wave packet resides. The altitude at which the magnitude of the momentum flux is maximum is referred to as the dissipation altitude [*Vadas and Fritts*, 2005]. This is the point where the diffusivity becomes large enough to overtake the growth of the wave due to decreasing background density. Table 2 shows the dissipation altitudes and peak altitude of wind velocity for each forcing. We also obtain an estimation of the dissipation altitude from a full-wave model (FWM) [*Hickey et al.*, 1998] which agrees well with our model, suggesting a dissipation altitude of 124 km compared to our 129 km; however, our solution does oscillate slightly about its steady state. These peak altitudes indicate the altitude at which dissipation effects become significant.

Figure 8 shows the plot of the altitude of the peak momentum flux, perturbation horizontal wind (u'), and vertical wind (w') with time. Three lines are plotted for each of the three forcings: the momentum flux peak (as defined above), the horizontal wind peak (calculated by averaging the absolute horizontal wind over a horizontal wavelength), and the vertical wind peak (calculated by averaging the absolute vertical wind over a horizontal wavelength). Since the horizontal and vertical winds vary throughout the spectrum, the altitudes where they achieve maximum values are time dependent.

For the quasi-monochromatic forcing, the momentum flux peaks at 129 km at ~350 min. It is at this time that the molecular viscosity acts to reduce the absolute amplitude of the wave and dissipation really takes hold. For the steady state case, the momentum flux peak levels out at 123 km altitude between 260 and 347 min. Here the wave enters the stable region of the lower thermosphere, and its vertical wavelength shrinks, reducing its vertical group velocity. The wave exits this region at 350 min and then continues to propagate upward until it reaches its dissipation altitude at 450 min (at an altitude of 129 km), at this stage the solution begins to oscillate slightly about its steady state, due to the time-dependent nature of the simulation and reflections within the domain.

Note that while these plots tell us the altitude of the dominant portion of the wave spectrum at any given time, the absolute peak in the momentum flux altitude does not necessarily correspond to the time when the spectral intensity and thus momentum flux is maximum. A clear example of this is the case of the spectrally broad forcing. Although the momentum flux peak altitude occurs at around 140 min (166 km), we can see from Figure 6b that the spectral intensity is actually maximum at ~ 175 min (where the momentum flux height drops to 159 km, these are the values quoted in Table 2). This occurs because of the changing dominant frequency component of the packet with time and is particularly prominent for the spectrally broad packet. The decrease in altitude of the momentum flux peak is a direct result of the selective dissipation of the higher (to progressively lower) frequency components of the packet with time. At 140 min, the dominant period is 16 min; hence, this part of the wave packet propagates higher, faster, and dissipates earlier than the 19.6 min period component which then becomes dominant at the time of peak spectral intensity.

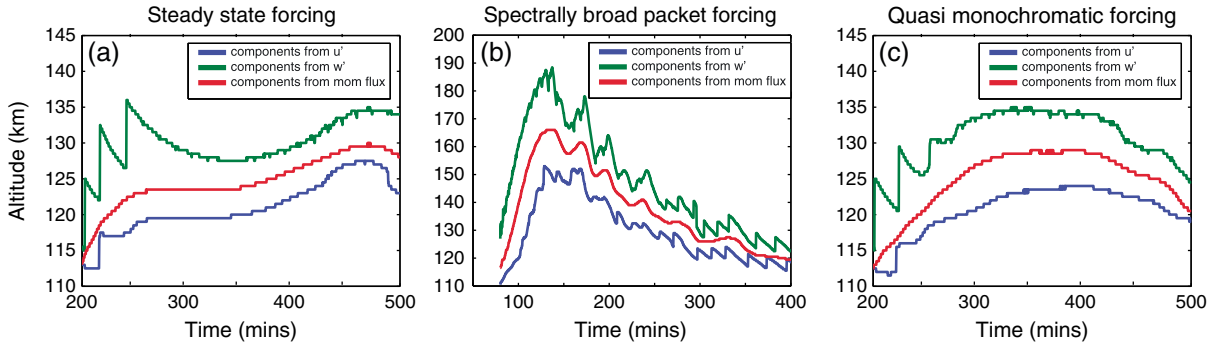

Figure 8. (a–c) Altitudes of the maximum values of the momentum flux, horizontal, and vertical winds as a function of time, shown for all three time-dependent forcing case studies.

3.4. Wavelet Analysis of Frequency Components

In order to study the frequency components of each forcing as a function of both time and space, a wavelet analysis was performed on the modeled horizontal wind. We utilize a wavelet analysis as described in *Torrence and Compo* [1998] using their software (http://paos.colorado.edu/research/wavelets/). We perform a convolution between a Morlet wavelet of varying period scales, ranging from 0.5 to 630 min, and the data set, while sliding it along in time, to assess the frequency components of the data set. This allows us to measure the frequency components as a function of altitude as well as time. When utilizing this method, we are able to look at localized regions and probe a range of scales rather than looking at the whole domain via standard Fourier analysis.

The analysis was performed in one dimension, so we take values at $x = 50$ km with time and produce a single time series plot of wind velocity for each altitude. The wavelet analysis is then performed on each of these data series, producing a plot of period and time.

We then take the dominant period component within the cone of influence, which denotes the maximum useful period without edge effects, at each time, for each altitude. The result gives a time, altitude, and dominant period plot related to the x, y, and z axes, respectively, as shown in Figure 9. Doing this allows us to compare the frequencies present within the model, with the change in vertical wavelength over time as shown in Figures 5–7. In the region shown in the Figure 9a (steady state forcing), there are three-period components present over the time and altitude plotted (subject to limitations of temporal resolution). Beyond 417 min, the entire domain shows a single dominant period component (27.8 min); it is here that the simulation is near to its steady state. Comparing this to Figure 5b, we see that the increase in negative vertical wave number occurs simultaneously (also 417 min) with the change in dominant period from the 33 min period (lighter blue) to the 27.8 min period (darker blue). Also from Figure 8a, we see that the wind peak occurs at the altitude (122 km) where the period component change occurs (at a time of 417 min).

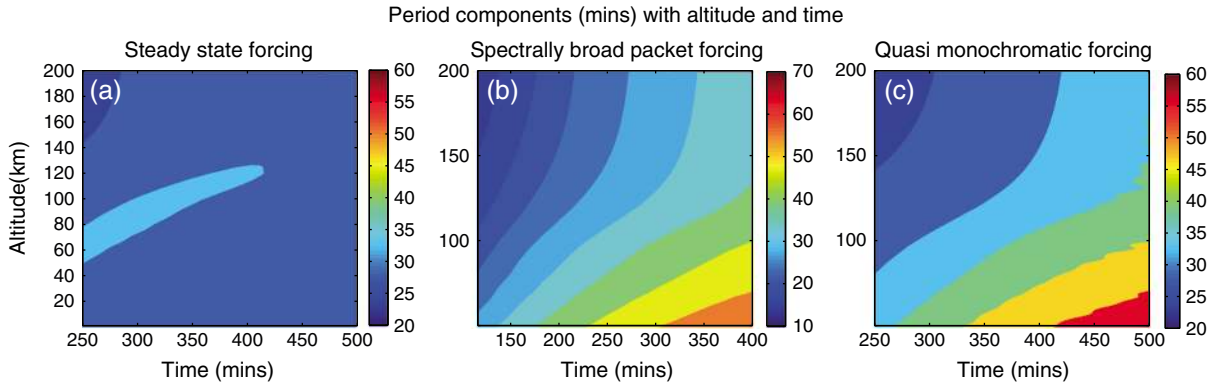

Figure 9. (a–c) The dominant period (denoted by the color) as a function of time and altitude. Shown for all three time-dependent forcing case studies, taken from the modeled horizontal wind perturbations.

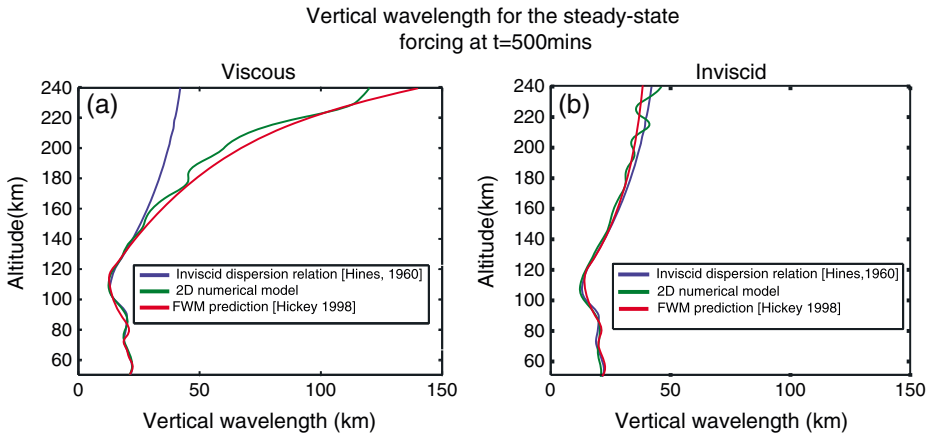

Figure 10. The vertical wavelength with altitude for the steady state forcing case, after reaching approximate steady state, for cases (a) with viscosity and (b) without. Comparisons with the Hines inviscid dispersion relation and with the *Hickey et al.*'s [1998] FWM are included.

Figure 9b, corresponding to the spectrally broad packet forcing, shows a much larger range of dominant periods throughout the domain. At any given altitude, the dominant period component increases in time, which for a fixed horizontal wavelength, would mean an increase (decrease) in vertical wave number (wavelength) under the assumption of the classical Hines inviscid dispersion relation.

Figure 9c shows the dominant period components in the quasi-monochromatic forcing case. As expected, this result is intermediate between the two former cases. The period spectrum throughout the domain is broader than the steady state case but narrower than the spectrally broad packet case. In Figure 7b, there is a jump (within our time resolution) at both 325 and 454 min in the vertical wavelength derived from the horizontal wind. At these times, Figure 8c shows that the altitude of the maximum amplitude as determined from the horizontal wind is 122 km. This jump in vertical wavelength can be explained by the change in dominant frequency. Figure 9c shows that at 122 km, the frequency changes from 27.80 to 33.06 min at $t = 325$ min and from 33.09 to 39.00 min at $t = 454$ min.

3.5. Vertical Wavelength With Altitude

For the steady state (single frequency) case, we calculate the vertical wavelength with altitude by measuring the lines of constant phase directly from the simulation. This is done by finding the horizontal grid position at which the wave velocity is maximum, for each altitude. The horizontal grid location is plotted as a function of altitude to give us a curve of constant phase for a given time t. Once we have the lines of constant phase, we take a tangent to the curve at each altitude. Since the horizontal wavelength is fixed throughout the simulation, multiplying the tangent to the curve $\frac{\delta\lambda_z}{\delta\lambda_x}$ by the horizontal wavelength $\lambda_x = 100$ km, will give us an approximate value of the vertical wavelength (λ_z) at each altitude, where the resolution is limited by our grid size to 0.5 km.

We compare our measured vertical wavelengths with the prediction made by the anelastic version of the *Hines* [1960], inviscid dispersion relation [*Gossard and Hooke*, 1975] given by

$$\omega_I^2 = \frac{k^2N^2}{m^2 + k^2 + 1/4H^2} \tag{13}$$

where ω_I is the intrinsic frequency and taken to be $2\pi/30$ min, N is the buoyancy frequency, m is the vertical wave number, k is the horizontal wave number (taken to be $2\pi/100$ rads/km^{-1}), and H is the density scale height. In addition, we compare our steady state result with that of *Hickey et al.*'s [1998] FWM. Figure 10 shows the vertical wavelength as a function of altitude taken at a time when the simulation exhibits steady state behavior for both the viscous and inviscid cases. The (viscous) steady state forcing agrees very well with the FWM prediction model. For the inviscid case, the vertical wavelength agrees well with the Hines dispersion relation and FWM, with some fluctuations apparent at high altitudes due to interaction with the

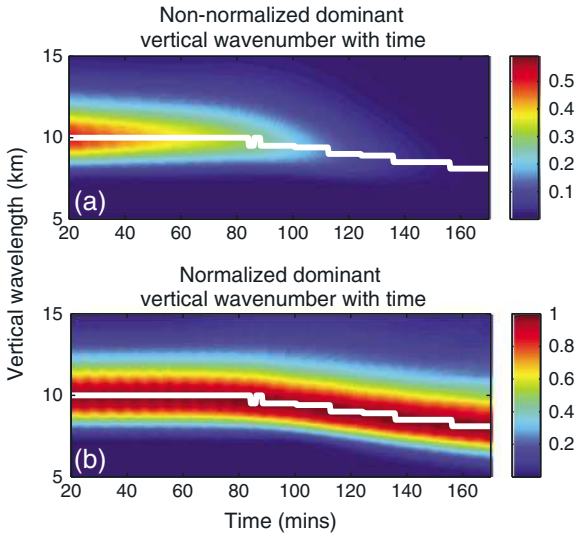

Figure 11. The temporal evolution of the vertical wavelength spectra for the isothermal simulation. Panel (a) shows the non-normalized spectra and panel (b) shows the spectra which has been normalized to the maximum value at each time. The overplotted white line denotes the maximum spectral intensity with time.

upper boundary of the model. We note that the momentum flux peak occurs at an altitude of 129 km in the viscous steady state case, which is where the wave dissipation begins to cause a divergence between the prediction based on the Hines inviscid dispersion relation and the prediction based on simulations that include viscous effects. We do not see a decrease in vertical wavelength in altitude above the dissipation altitude, at any fixed time, but we do note that background temperature variations play a significant role in the wave's vertical structure. However, this is accounted for in the vertical wavelength prediction of Hines; thus, any difference between that and the simulation results and FWM prediction should be due to the effect of viscosity.

4. Comparison With Previous Studies

4.1. Isothermal Initial Condition Run

The previous simulations incorporated a realistic background temperature structure, which contributes to the altitude dependence of vertical wavelength. In order to look at a more simplified case, we perform an isothermal simulation, with an initial wave condition specified within the horizontal wind field. For the purpose of providing a direct comparison, this simulation is based upon parameters provided by *Liu et al.* [2013], which specify a well-defined packet under isothermal conditions. In particular, we recreate Figure 4 using case B from *Liu et al.* [2013, Table 1]. The parameters used are $T = 239$ K, γ=1.4, $R = 287$ J kg^{-1} K^{-1}, $\lambda_x = 20$ km, $\lambda_z = 10$ km, $\tau_{gw} = 11.76$ min. The scale height is taken to be 7 km, and the buoyancy frequency is 0.02 radius s^{-1}.

The horizontal velocity perturbation is given by

$$u'(x,z,t=0) = A\exp\left[-\ln(2)\frac{(z-z_0)^2}{2\sigma_z^2}\right]\exp\left(\frac{z-z_0}{2H}\right) \cdot \cos\left[k_x x + k_z(z-z_0)\right] \tag{14}$$

where $A = 1.0\times10^{-3}$ m/s, $z_0 = 60$ km, $\sigma_z = 10$ km $= \lambda_z$, and the other perturbation quantities are derived using the polarization relations as set out in *Fritts and Alexander* [2003]. The gravity waves are density weighted by the term $(\rho_0(z)/\rho_0(z_r))^{1/2}$ where $z_r = 60$ km. The kinematic molecular viscosity is given as

$$\nu(z) = 3.5\text{x}10^{-7}T(z)^{0.69}/\rho(z) \tag{15}$$

The differences between our simulation and that of *Liu et al.* [2013] are that we did not use a Raleigh friction term. We use only the dissipation processes included in *Vadas and Fritts* [2005], and our domain was only 20 km × 170 km with horizontal and vertical resolutions of 0.5 km. Our time step was also longer at a value of 0.8 s.

In recreating Figure 4b from *Liu et al.* [2013] we highlight an important difference. *Liu et al.* [2013] take the vertical wavelength spectrum and normalize it to the maximum power at each time. The resulting plot, recreated here in Figure 11b, shows a slope beginning at about 100 min that indicates a decreasing (increasing) vertical wavelength (wave number) with increasing time. Figure 11a shows the result of the power spectrum without normalization. In this case, the bottom portion (higher-$|m|$ portion) of the spectrum remains nearly constant with time, while the spectral power tapers off from the top (lower-$|m|$

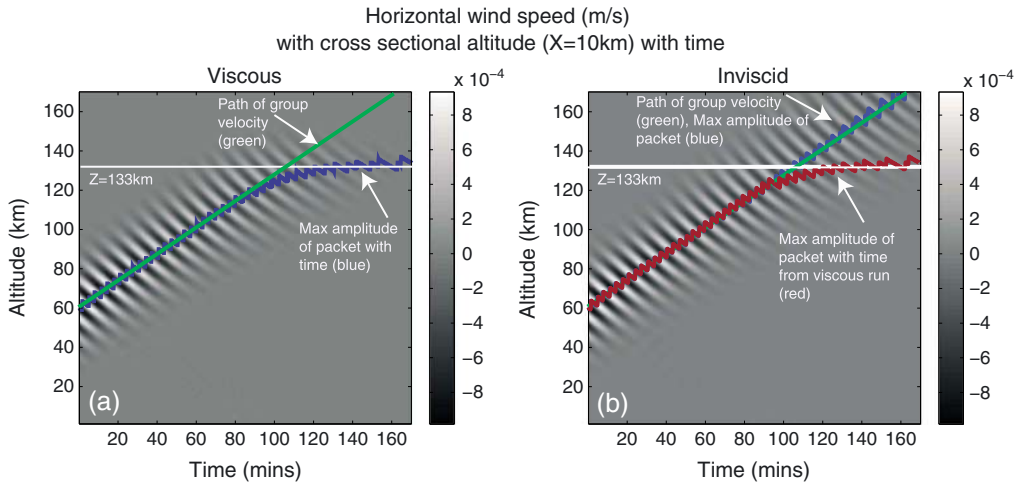

Figure 12. Figure shows a time evolution of the horizontal wind (at $x = 50$ km) for (a) the viscous case and (b) the inviscid case, with paths defined by (1) the maximum amplitude of the packet (blue), (2) the group velocity as defined by Hines [1960] (green), and (3) the maximum amplitude from the viscous case overlaid on the inviscid case (red).

portion), indicating that the higher frequency (longer wavelength) components are dissipating away first as time progresses. This is the same mechanism as had previously been suggested in this paper. Although there is still a small shift in the vertical wave number spectrum toward higher wave numbers, perhaps indicating a decrease in vertical wavelength with time due to dissipation, the initial and dominant effect appears to be the selective dissipation of the higher frequency components within the packet; essentially, the waves that arrive first are removed first.

In order to substantiate this claim, we produce two additional plots. Figure 12 is similar to Figure 4 but also includes various "ray" paths overlaid for (a) a viscous case and (b) an inviscid case. The overlaying blue line shows the path taken by the maximum wind amplitude of the packet in time, which corresponds to the dominant frequency components in the Fourier transforms of Figure 11a. The vertical wavelength is derived (using the same method as section 3.5) along this path and plotted as the blue line seen in Figure 13a for the viscous case. We see, as with the Fourier analysis, that the vertical wavelength decreases from 10 km to 8.2 km between 90 and 150 min when viscosity is present. This time period corresponds to when the packet is strongly dissipating, and it ceases to propagate vertically (beyond $z = 133$ km) and instead appears to propagate in a purely horizontal direction (see Figure 12a). However, if we take a horizontal slice at $z = 133$ km (as denoted by the white line in Figure 12 and plotted in Figure 13c), it is clear that we are seeing different parts of the packet spectrum as time progresses. At $t = 100$ min the approximate period of the wave is 11.2 min, but by 120 min it has increased to approximately 13 min. Using the Hines (inviscid) dispersion relation for these approximate periods, we obtain vertical wavelength values of 10.6 and 8.84 km, respectively. While these values are only estimates, they are, nonetheless, consistent with the decrease in vertical wavelength simulated earlier. This supports our claim that the dominant effect observed in packet dissipation is the decrease of vertical wavelength in time, due to the initial dominance of the higher frequency (longer wavelength) which travel faster and dissipate first, giving way to the lower frequency (shorter wavelength) components of the packet.

In addition, we plot the trajectory of the packet as predicted by the group velocity of the central frequency and wavelength of the packet, and shown by the green line in Figure 12. The group velocity used was that derived from the Hines inviscid relation and given by

$$V_{gz} = \frac{-m\omega^2}{\omega(k^2 + m^2 + \frac{1}{4H^2})} \tag{16}$$

We then plot the vertical wavelength with time along this vertical trajectory (Figure 13a, green line) and find that the vertical wavelength increases around the same time that the vertical wavelength measured by the maximum amplitude of the packet begins to decrease. This occurs because, while the packet dissipates

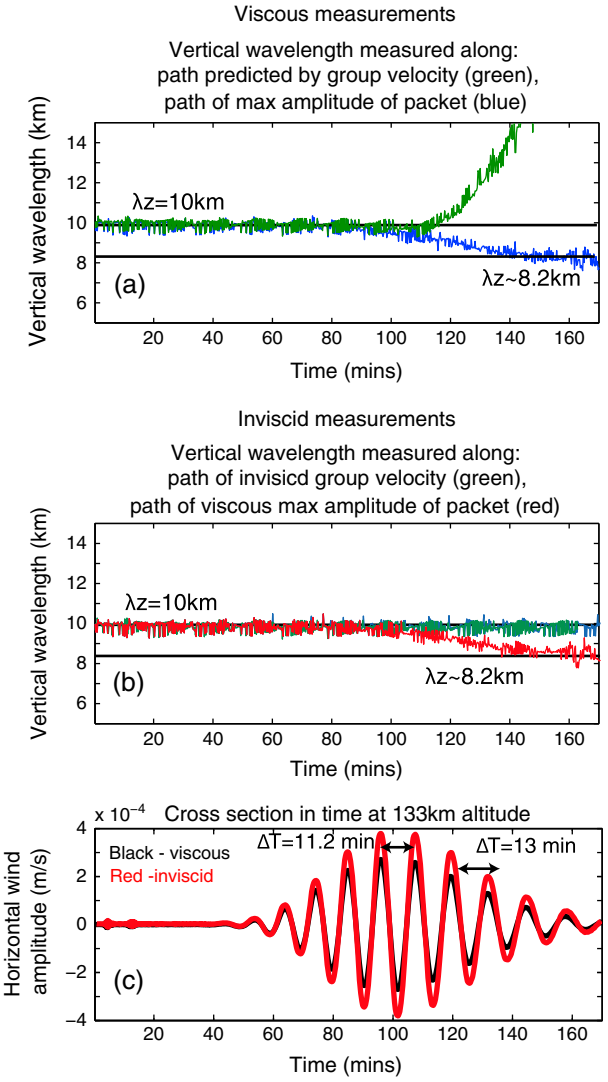

Figure 13. (a) The vertical wavelengths measured along the corresponding paths in Figure 12a. (b) The vertical wavelengths measured along the corresponding paths in Figure 12b. (c) A horizontal slice at $z = 133$ km for the viscous (black) and inviscid (red) cases.

and its upward trajectory ceases, the trajectory described by the inviscid group velocity continues upward and thus passes through the higher-frequency (longer wavelength) portions of the packet which are able to reach higher altitudes before dissipating.

In the inviscid case, the trajectory traced out by the maximum amplitude of the packet and that of the group velocity are the same since the molecular viscosity and thermal conductivity are not there to halt the upward propagation of the wave packet. Even though this was specified as a quasi-monochromatic initial condition source in both *Liu et al.* [2013] and in our simulations, there is a clear dispersion of the packet as it propagates upward. Figure 13b shows, as we would expect, that the vertical wavelength remains approximately constant along the group path when no viscous effects are present. Figure 13c shows the horizontal wind amplitudes as a function of time at $z = 133$ km (where the packet ceases its upward propagation) for the viscous and inviscid cases. It can be seen that the wave packet is almost exactly the same except for a decrease in amplitude in the viscous case. This suggests that it is essentially the "cutting off" of the dominant (central frequency and wave number) part of the packet by dissipation above 133 km which causes the maximum amplitude of the packet to migrate to the lower frequency components of the packet (and hence cause the cessation of the upward trajectory of the packet). In order to emphasize this point, we overlay the path of the maximum wind amplitude from the viscous case (Figure 12a, blue line) onto the inviscid case and derive the inviscid vertical wavelength along this same path (Figure 12b, red line). We see that there is very little difference between the measured vertical wavelength along this same path in the viscous and inviscid simulations. This suggests strongly that the decrease in vertical wavelength, seen in the viscous case in Figure 12a, is an effect created by the time-dependent dissipation of the different frequencies within a packet.

5. Discussion and Conclusions

Using a 2-D nonlinear and compressible model [*Snively and Pasko*, 2008], we simulated gravity wave packets generated by three separate forcings, to investigate the dissipation of wave packets of different spectral content. Our three forced simulations consisted of (1) a steady state, (2) a spectrally broad packet forcing, and (3) a quasi-monochromatic packet, each with a period of 30 min and horizontal wavelength of 100 km. In addition, we simulated gravity waves specified as an initial condition in an isothermal background atmosphere.

The amplitude was small enough to ensure that all interactions were approximately linear, and no background winds were specified.

We investigated the time evolution of the vertical wave number spectrum in each case and found that the dominant vertical wavelength of the steady state simulation (1) remained at a constant value of 16 km after the transients passed. The other two cases (2 and 3) showed a steadily decreasing vertical wavelength with time as seen in previous studies [*Liu et al.*, 2013; *Zhang and Yi*, 2002]. The spectrally broad packet showed the greatest change in vertical wavelength with time and highlighted the fact that the earlier dissipation of higher-frequency wave components can lead to an observed decrease in vertical wavelength. The quasi-monochromatic packet also exhibited a decrease in vertical wavelength in time which could be attributed to the temperature structure, earlier dissipation of higher frequency components in time, and perhaps the direct effect of dissipation shortening the vertical wavelength, as suggested by *Vadas and Fritts* [2005].

A wavelet analysis, following the methods of *Torrence and Compo* [1998], was used to determine the dominant period components of each simulation in both time and space. As expected, we identify a broad-period spectrum in the spectrally broad packet case which contributes to the large change in vertical wavelength with time. In the steady state case we see only one significant change in vertical wavelength, corresponding to a change in dominant period as identified in the wavelet analysis. At late times, one component is clearly dominant. In the quasi-monochromatic case, we attribute two large changes in the vertical wavelength in time, to changes in the dominant period.

We compared the results of our studies with previous studies utilizing other models including time-dependent simulations by *Liu et al.* [2013] and *Zhang and Yi* [2002] and steady state models [*Hickey et al.*, 1998]. In particular, we find that the dissipation altitude matches very well with that derived from simulations using the *Hickey et al.*'s [1998] FWM for the steady state case, and with *Liu et al.* [2013] for the initial condition case studies. In the steady state case, the variation with altitude of the vertical wavelength show good agreement with the Hines prediction up to the dissipation altitude (about 129 km altitude), diverging above as expected. The vertical wavelength agrees very well with the results of the FWM at altitudes above the dissipation height. We note that the vertical wavelength always increases with altitude above the dissipation altitude at an instant in time, as suggested in *Waterscheid and Hickey* [2011]. However, we also note that the background temperature structure has a strong effect on the vertical wavelength change with altitude, especially at altitudes where the wave amplitudes are still large.

For the initial condition-based run (4), we find that creating a normalized power spectrum at each time [e.g., *Liu et al.*, 2013] will lead to a general downward slope in the spectra suggesting a decrease in vertical wavelength. However, when the spectra are not normalized, they appear mostly flat in time except for a tapering from the long-wavelength part of the spectrum that we suggest is caused by the earlier dissipation of high frequency components, with high vertical group velocities, by the thermosphere. Further analysis shows that when tracking the vertical wavelength with time along the trajectory traced out by the maximum wind amplitude of the packet, the decrease in wavelength is consistent with the increasing dominant period of the wave packet as the higher frequencies dissipate away. By comparing with an inviscid case, we suggest that the dominant portion of the packet is essentially "cut off" by dissipation above 133 km causing the dominant portion of the packet to move to the lower frequencies and cause the trajectory to become nearly horizontal. Essentially, the most important reason for the decrease in vertical wavelength in time occurs because the waves that arrive first (the higher frequency, longer wavelength components of a packet) are removed first.

In conclusion, we suggest that the decrease in dominant vertical wavelength of the simulated packets (when not continuously forced) in time, is predominantly due to the selective dissipation of the higher-frequency packet components and the change of temperature with altitude via the following mechanism. The faster, longer λ_z parts of the packet propagate upward, with amplitude increasing as $\sim e^{\frac{z}{2H}}$. They reach an altitude (dissipation altitude) where dissipation overtakes growth, and at greater heights their amplitude decays. They are followed by the slower, shorter λ_z components that experience greater dissipation rates than the faster waves, and hence, their dissipation altitudes are lower. The result is that faster waves of large λ_z travel higher into the thermosphere but dissipate first and are then replaced by the slower waves of shorter λ_z. Thus, from a time-dependent stand point, the vertical wavelength of the packet appears to decrease. However, at any fixed time, the vertical wavelength appears to increase with increasing altitude.

We do not rule out that dissipation can decrease the vertical wavelength of a single frequency component [e.g., *Vadas and Fritts*, 2005; *Vadas*, 2007]; however, it is not a dominant effect in determining the evolutions of the packet spectra simulated here.

Most importantly, comparisons of the wave forcing types highlight how differently a wave packet can behave depending upon how it is specified or defined. Assumption of a single central frequency, wave number, and packet location is insufficient to characterize a spectrally broad packet due to the strong dispersion effects and selective filtering of the differing frequency components present. Conversely, in steady state situations, a wave is constantly forced at a single frequency which is present throughout the domain. As such, its dissipation altitude is much better described by treating it as having a single central frequency and wave number.

Acknowledgements

Research by C.J. Heale, C.J. Ali, and J.B. Snively was supported under NSF grants AGS-1113427 and AGS-1151746. Research by M.P. Hickey was supported under NSF AGS-1001074. The authors thank Sharon Vadas and an anonymous reviewer for their helpful comments.

Robert Lysak thanks Sharon Vadas and an anonymous reviewer for their assistance in evaluating this paper.

References

Djuth, F. T., M. P. Sulzer, S. A. Gonzeles, J. D. Mathews, J. H. Elder, and R. L. Walterscheid (2004), A continuum of gravity waves in the arecibo thermosphere, *Geophys. Res. Lett.*, *31*, L16801, doi:10.1029/2003GL019376.

Einaudi, F., and C. O. Hines (1971), WKB approximation in application to acoustic-gravity waves, *Can. J. Phys.*, *48*, 1458–1471.

Francis, S. H. (1973), Acoustic-gravity modes and large scale traveling ionospheric disturbances of a realistic, dissapitive atmosphere, *J. Geophys. Res.*, *78*, 2278–2301.

Fritts, D., and M. J. Alexander (2003), Gravity wave dynamics and effects in the middle atmosphere, *Rev. Geophys.*, *41*(1), 1003, doi:10.1029/2001RG000106.

Fritts, D. C., and T. S. Lund (2011), Gravity wave influences in the thermosphere and ionosphere: Observations and recent modeling, in *Aeronomy of the Earth's Atmosphere and Ionosphere*, edited by M. A. Abdu, D. Pancheva, and A. Bhattacharyya, pp. 109–130, Springer, New York.

Fritts, D. C., S. L. Vadas, K. Wan, and J. A. Werne (2006), Mean and variable forcing of the middle atmosphere by gravity waves, *J. Atmos. Sol. Terr. Phys.*, *68*, 247–265.

Gossard, E. E., and W. H. Hooke (1975), *Waves in the Atmosphere*, 456 pp., Elsevier, New York.

Hedin, A. E. (1991), Extension of the MSIS thermosphere model into the middle and lower atmosphere, *J. Geophys. Res.*, *96*(A2), 1159–172.

Hickey, M. P., M. J. Taylor, C. S. Gardner, and C. R. Gibbons (1998), Full-wave modeling of small-scale gravity waves using Airborne Lidar and Observations of the Hawaiian Airglow (ALOHA-93) O(1S) images and coincident Na wind/temperature lidar measurements, *J. Geophys. Res.*, *103*(D6), 6439–6453.

Hickey, M. P., R. L. Walterscheid, and G. Schubert (2010), Wave mean flow interactions in the thermosphere induced by a major tsunami, *J. Geophys. Res.*, *115*, A09309, doi:10.1029/2009JA014927.

Hickey, M. P., R. L. Walterscheid, and G. Schubert (2011), Gravity wave heating and cooling of the thermosphere: Roles of the sensible heat flux and viscous flux of kinetic energy, *J. Geophys. Res.*, *116*, A12326, doi:10.1029/2010JA016792.

Hines, C. (1960), Internal atmospheric gravity waves at ionospheric heights, *Can. J. Phys.*, *38*, 1441–1481.

Hocke, K., and T. Tsuda (2001), Gravity waves and ionospheric irregularities over tropical convection zones observed by GPS/MET radio occultation, *Geophys. Res. lett.*, *28*, 2815–2818.

Hung, R. J., and J. P. Kuo (1978), Ionospheric observations of gravity-waves associated with Hurricane Eloise, *J. Geophys. Res.*, *45*, 67–80.

Kelley, M. C. (1997), In situ ionospheric observations of severe weather-related gravity waves and associated small-scale plasma structure, *J. Geophys. Res.*, *102*, 329–336.

LeVeque, R. J., and M. J. Berger (2004), *Clawpack software version 4.6*. www.clawpack.org.

Liu, X., J. Xu, J. Yue, and S. L. Vadas (2013), Numerical modeling study of the momentum deposition of small amplitude gravity waves in the thermosphere, *Ann. Geophys.*, *31*, 1–14.

Oliver, W., Y. Otsuka, M. Sato, T. Takami, and S. Fukao (1997), A climatology of f region gravity wave propagation over the middle and upper atmosphere radar, *J. Geophys. Res.*, *102*, 14,499–14,512.

Pitteway, M. L. V., and C. O. Hines (1963), The viscous damping of atmospheric gravity waves, *Can. J. Phys.*, *41*, 1935–1948.

Rees, M. (1989), *Physics and Chemistry of the Upper Atmosphere*, Cambridge Univ. Press, Cambridge.

Snively, J. B. (2013), Mesospheric hydroxyl airglow signatures of acoustic and gravity waves generated by transient tropospheric forcing, *Geophys. Res. Lett.*, *40*, 4533–4537, doi:10.1002/grl.50886.

Snively, J. B., and V. P. Pasko (2008), Excitation of ducted gravity waves in the lower thermosphere by tropospheric sources, *J. Geophys. Res.*, *113*, A06303, doi:10.1029/2007JA012693.

Torrence, C., and G. P. Compo (1998), A practical guide to wavelet analysis, *Bull. Am. Meteorol. Soc.*, *79*(1), 61–78.

Vadas, S. L. (2007), Horizontal and vertical propagation and dissipation of gravity waves in the thermosphere from lower atmospheric and thermospheric sources, *J. Geophys. Res.*, *112*, A06305, doi:10.1029/2006JA011845.

Vadas, S. L., and D. C. Fritts (2005), Thermospheric responses to gravity waves: Influences of increasing viscosity and thermal diffusivity, *J. Geophys. Res.*, *110*, D15103, doi:10.1029/2004JD005574.

Vadas, S. L., J. Yue, C. Y. She, P. A. Stamus, and A. Z. Liu (2009), A model study of the effects of winds on concentric rings of gravity waves from a convective plume near Fort Collins on 11 May 2004, *J. Geophys. Res.*, *114*, D06103, doi:10.1029/2008JD010753.

Vadas, S. L., and H. L. Liu (2009), Generation of large scale gravity waves and neutral winds in the thermosphere from the dissipation of convectively generated gravity waves, *J. Geophys. Res.*, *114*, A10310, doi:10.1029/2009JA014108.

Vadas, S. L., and H. L. Liu (2013), Numerical modeling of the large-scale neutral and plasma responses to the body forces created by the dissipation of gravity waves from 6 h of deep convection in Brazil, *J. Geophys. Res. Space Physics*, *118*, 2593–2617, doi:10.1002/jgra.50249.

Vadas, S. L., and M. J. Nicolls (2012), The phases and amplitudes of gravity waves propagating and dissipating in the thermosphere: Theory, *J. Geophys. Res.*, *117*, A05322, doi:10.1029/2011JA017426.

Walterscheid, R. L., and M. P. Hickey (2001), One-gas models with height-dependent mean molecular weight: Effects on gravity wave propagation, *J. Geophys. Res.*, *106*, 28,831–28,839, doi:10.1029/2001JA000102.

Walterscheid, R. (2013), The propagation of transient wave packets in highly dissipative media, *J. Geophys. Res. Space Physics*, *118*, 878–884, doi:10.1002/jgra.50097.

Waterscheid, R. L., and M. P. Hickey (2011), Group velocity and energy flux in the thermosphere: Limits on the validity of group velocity in a viscous atmosphere, *J. Geophys. Res.*, *116*, D12101, doi:10.1029/2010JD014987.

Yigit, E., A. D. Aylward, and A. S. Medvedev (2008), Parameterization of the effects of vertically propagating gravity waves for thermosphere general circulation models: Sensitivity study, *J. Geophys. Res.*, *113*, D19106, doi:10.1029/2008JD010135.

Yigit, E., A. S. Medvedev, A. D. Aylward, P. Hartogh, and M. J. Harris (2009), Modeling the effects of gravity wave momentum deposition on the general circulation above the turbopause, *J. Geophys. Res.*, *114*, D07101, doi:10.1029/2008JD011132.

Yu, Y., M. Hickey, and Y. Liu (2009), A numerical model characterizing internal gravity wave propagation into the upper atmosphere, *Adv. Space Res.*, *44*(7), 836–846.

Zhang, S. D., and F. Yi (2002), A numerical study of propagation characteristics of gravity wave packets propagating in a dissipative atmosphere, *J. Geophys. Res.*, *107*(D14), 4222, doi:10.1029/2001JD000864.